PNAS RESEARCH ARTICLE | ENVIRONMENTAL SCIENCES

Fenton-like activity and pathway modulation via single-atom sites and pollutants comediates the electron transfer process

Jirui Guo[a], Yujie Wang[a], Yanan Shang[b,1], Kexin Yin[a], Qian Li[a], Baoyu Gao[a], Yanwei Li[c], Xiaoguang Duan[d], and Xing Xu[a,1]

Edited by Alexis Bell, University of California, Berkeley, CA; received August 8, 2023; accepted November 29, 2023

The studies on the origin of versatile oxidation pathways toward targeted pollutants in the single-atom catalysts (SACs)/peroxymonosulfate (PMS) systems were always associated with the coordination structures rather than the perspective of pollutant characteristics, and the analysis of mechanism commonality is lacking. In this work, a variety of single-atom catalysts (M-SACs, M: Fe, Co, and Cu) were fabricated via a pyrolysis process using lignin as the complexation agent and substrate precursor. Sixteen kinds of commonly detected pollutants in various references were selected, and their lnk_{obs} values in M-SACs/PMS systems correlated well (R^2 = 0.832 to 0.883) with their electrophilic indexes (reflecting the electron accepting/donating ability of the pollutants) as well as the energy gap (R^2 = 0.801 to 0.840) between the pollutants and M-SACs/PMS complexes. Both the electron transfer process (ETP) and radical pathways can be significantly enhanced in the M-SACs/PMS systems, while radical oxidation was overwhelmed by the ETP oxidation toward the pollutants with lower electrophilic indexes. In contrast, pollutants with higher electrophilic indexes represented the weaker electron-donating capacity to the M-SACs/PMS complexes, which resulted in the weaker ETP oxidation accompanied with noticeable radical oxidation. In addition, the ETP oxidation in different M-SACs/PMS systems can be regulated via the energy gaps between the M-SACs/PMS complexes and pollutants. As a result, the Fenton-like activities in the M-SACs/PMS systems could be well modulated by the reaction pathways, which were determined by both electrophilic indexes of pollutants and single-atom sites. This work provided a strategy to establish PMS-based AOP systems with tunable oxidation capacities and pathways for high-efficiency organic decontamination.

Fenton-like | single-atom catalyst | electron transfer | refractory organic contaminants

Significance

The origin of versatile oxidation pathways toward targeted pollutants in the single-atom catalysts (SACs)/peroxymonosulfate (PMS) systems is always identified from the coordination structures rather than from the perspective of pollutant characteristics. In this work, we report that the tunable electron transfer process (ETP) in M-SACs (M: Fe, Co, and Cu)/PMS systems is associated with the electron-donating capacity (as measured by electrophilic index) of different pollutants, which correlates well with their Fenton-like activities in M-SACs/PMS systems, thus affecting the respective contributions of ETP and radical pathways to the degradation of different pollutants. This work will be a significant contribution to the Fenton-like activity and pathway modulation of the SACs/PMS systems in the oxidation of different micropollutants.

In recent years, versatile refractory emerging micropollutants with complex and diverse properties have been frequently detected in various water and wastewaters, which brings great challenges to the remediation of water pollution and the recycling of water resources (1). Therefore, it is of vital importance to develop efficient and affordable water decontamination technologies, among which advanced oxidation processes (AOPs) aiming at complete destruction of various hazardous pollutants is an indispensable option (2–9). Among various AOPs, the peroxymonosulfate (PMS) based Fenton-like reaction has an excellent effect on removing recalcitrant pollutants in the aqueous phase (10–13). However, the existing catalysts have the fundamental obstacles of poor stability, low selectivity, and high treating cost, thus far limiting the practical application of traditional AOPs. In addition, the surface chemistry of catalysts is complicated and difficult for precise control, leading to the challenges in the identification of active sites and the analysis of catalytic mechanisms (14).

Single-atom catalysts (SACs) with nearly 100% metal-atom utilization and adjustable electronic structure have become one of the most promising catalysts for PMS-AOPs, and they have attracted much attention in recent years (6, 15–17). M-SACs with a transition metal (e.g., Co, Fe, Cu, or Mn) as the active center have attracted increasing interest for PMS activation (6, 15, 18–21). Co- and Fe-based SACs have been reported to be the most active catalysts (6, 15, 19). For example, Co- or Fe-based SACs with N-coordination even showed one order of magnitude higher efficiency than traditional nanomaterials for activation of PMS and elimination of the micropollutant bisphenol A (12, 22). In addition, regulating the coordination environment of the central metal sites in SACs has also become an important strategy to produce reactive species precisely and efficiently (15, 22–24). For example, the PMS-activation pathway by designing a Co–N_{2+2} conformation would trigger almost 100% of $^1O_2$ generation as compared with the radical-based Co–N_4/PMS system (23). The regulation of N numbers in SACs via controlling different calcination temperatures could also exhibit significantly different catalytic performances and catalytic pathways (15, 22).

Author contributions: J.G., Y.S., Q.L., B.G., X.D., and X.X. designed research; X.X. performed research; K.Y. contributed new reagents/analytic tools; J.G., Y.W., Y.S., K.Y., and Y.L. analyzed data; Q.L. and X.X. supervised the project; and J.G. wrote the paper.

The authors declare no competing interest.

This article is a PNAS Direct Submission.

[1] To whom correspondence may be addressed. Email: shangyanan@sdust.edu.cn or xuxing@sdu.edu.cn.

This article contains supporting information online at https://www.pnas.org/lookup/suppl/doi:10.1073/pnas.2313387121/-/DCSupplemental.

Basically, recent studies based on SACs/PMS systems mainly focus on different oxidation mechanisms caused by SACs with different coordination structures activating PMS to achieve efficient degradation of pollutants (3, 10, 12, 19, 22, 23). However, when various pollutants are oxidized by SACs/PMS systems with the same coordination structure, completely different catalytic mechanisms are reported in different literatures, which makes us confused about the mechanism analysis (3, 10, 12, 19, 22, 23). What is the source of these different catalytic mechanisms? Therefore, the oxidation properties and mechanisms of different SACs/PMS systems depend not only on the coordination structures of SACs (e.g., considering coordination number, metal center and metal-carrier interaction), it is also necessary to analyze the comodulation of target pollutants with the SACs/PMS system toward the oxidation performances/pathways. Although there are some studies that reported that the degradation performances of pollutants in the SACs/PMS system were associated with the half-wave potential ($\varphi_{1/2}$) of pollutants (3, 25), the selection of pollutants is not comprehensive enough, and it is still uncertain whether only considering $\varphi_{1/2}$ values of pollutants are universal. The detecting factors as well as some organics due to the retarded oxidation peaks would inevitably affect the detection of their $\varphi_{1/2}$ values. In addition, several studies have reported a relationship between the electrophilic/nucleophilic indexes of pollutants and free radical attack (26, 27). However, these studies mostly focused on predicting the attacking sites of the pollutants by their electrophilic/nucleophilic indexes or considering the effects of free radical and nonradical synergies on the degradation of pollutants (26, 27). Few studies considered the effect of electrophilic indexes/nucleophilic index of different pollutants on Fenton-like reactions and oxidation pathways under the synergies of free radical and nonradical oxidation. Furthermore, the universality of electrophilic or nucleophilic indexes of various pollutants as well as the consequence with their degradation efficiency and mechanisms in versatile SACs/PMS systems was still unclear. Therefore, it is of great significance to establish the relationship between specific characteristics (e.g., $\varphi_{1/2}$, electrophilic index, and nucleophilic index) of pollutants and the oxidation kinetics/pathways in the SACs/PMS systems.

Basically, the aim of this study was to illustrate the Fenton-like activity and pathway modulation toward targeted pollutants in the SACs/PMS systems from the pollutant perspective. Three kinds of M-SACs (Fe-SAC, Co-SAC, and Cu-SAC) were fabricated via a pyrolysis process using iron, cobalt, and copper salts as metal precursors and the lignin as the parent material. Sixteen kinds of commonly used pollutants in various references were selected and their specific parameters (e.g., $\varphi_{1/2}$, electrophilic index and nucleophilic index) were evaluated. The relationship between their specific parameters and oxidation performances of pollutants in versatile M-SACs/PMS systems was further determined. Density functional theory (DFT) calculations were employed to investigate the energy gaps between the target pollutants and M-SACs/PMS complexes. Moreover, the transformation products of pollutants and the degradation performances in catalytic membrane systems were also assessed. This work brings an in-depth understanding on the modulation of Fenton-like activities and pathways in SACs/PMS systems via pollutants comediation.

Results and Discussions

Characterizations of the Catalysts. The fabrication scheme of various M-SACs (Fe-SAC, Co-SAC, and Cu-SAC) by using lignin as the precursor was shown in Fig. 1*A*. The lignin could be an excellent metal capturer for the dispersion of metal atoms in these M-SACs via the adsorption of metal ions by its hydroxy groups. The metal contents in the resulting M-SACs were 1.75 wt.% for Fe-SAC, 1.66 wt. % for Co-SAC, and 1.97 wt.% for Cu-SAC (*SI Appendix,* Table S1). XRD patterns of these M-SACs as well as the nitrogen-doped carbon catalyst (N-C) derived from iron-free lignin were given in Fig. 1*B*. The XRD patterns of these M-SACs were similar to that of N-C, and no specific peaks toward the metal nanoparticles can be observed, which confirmed that the anchored metal species have been successfully transferred into the Fe, Co or Cu single atoms in the lignin-based precursor. Raman spectra of these M-SACs also showed similar structures compared to that of N-C (*SI Appendix,* Fig. S1). In addition, uniformly dispersed spots can be visualized in the HAADF-HRTEM images of Fe-SAC, Co-SAC, and Cu-SAC (Fig. 1 *C–E*), which can be ascribed to the atomically dispersed metal atoms. This was further confirmed by the HAADF HRTEM mappings of M-SACs with well distributions of metal (Fe, Co, and Cu) species (Fig. 1 *C–E*). The XPS N1s of these M-SACs (Fe-SAC, Co-SAC, and Cu-SAC) showed a slight shift for the pyridinic N fraction as compared with the N-C (Fig. 1*F* and *SI Appendix,* Table S2), while no shift can be observed for graphitic N and pyrrolic N in the as-resulting catalysts. This result indicated that the metal atoms were coordinated with the pyridinic N to form the M-N (M: Fe, Co, and Cu) configurations. The coordination information of these M-SACs can be illustrated by the X-ray absorption fine structure (XAFS) analysis (24). For example, the Fe K-edge X-ray absorption near-edge structure (XANES) analysis of Fe-SAC showed that the Fe state of Fe-SAC was located between FeO and Fe_2O_3 (Fig. 1*G*). The extended X-ray absorption fine structure (EXAFS) showed that the coordination structure of Fe-SAC was based on $Fe\text{-}N_4\text{-}C$ configuration without the existence of Fe-Fe bonds (Fig. 1*J*, and *SI Appendix,* Figs. S2 and S3 and Table S3). Similar coordination information also confirmed the $Co\text{-}N_4\text{-}C$ configuration for Co-SAC and $Cu\text{-}N_4\text{-}C$ configuration for Cu-SAC (Fig. 1 *H–L* and *SI Appendix,* Figs. S2 and S3 and Table S3). In addition, wavelet transform (WT) contour plots of these M-SACs were quite similar to M-Pc with a well-defined $M\text{-}N_4$ coordination, but was significantly different from those of other metal species, e.g., metal foils, and metal oxides (Fig. 1*M* and *SI Appendix,* Fig. S4). These results further indicated the absence of M-M bonds (M: Fe, Co, and Cu) in the resulting M-SACs.

Relationship between Degradation Performances and Properties of Pollutants. Degradation of 16 kinds of pollutants (*SI Appendix,* Fig. S5), including paracetamol (PCM), bisphenol A (BPA), p-chlorophenol (CP), naproxen (NPX), hydroxybenzoic acid (HBA), carbamazepine (CBZ), ciprofloxacin (CIP), chlorotetracycline (CTC), nitrobenzene (NB), tetracycline (TC), sulfamethazine (SMT), sulfanilamide (SA), sulfamethoxazole (SMZ), p-nitrophenol (NP), chloramphenicol (CPL), and nithbenzoic acid (NBA) by different M-SACs/PMS systems (Fe-SAC/PMS, Co-SAC/PMS, and Cu-SAC/PMS), was shown in *SI Appendix,* Figs. S6–S8 and Fig. 2*A*. Three kinds of degradation trends via the classification of k_{obs} values can be observed toward these pollutants. For example, the pollutants (e.g., PCM, BPA, CP, NPX, SN, HBA, SMZ, and SMT) with electron-donating groups such as hydroxyl and amido groups could be easily oxidized in the Fe-SAC/PMS system with k_{obs} higher than 0.4 min^{-1}, while the pollutants (e.g., NB, CPL, and NBA) with electron-withdrawing groups (e.g., nitro group) were inert and difficult to be oxidized in the Fe-SAC/PMS system (<0.1 min^{-1}). The pollutants with both electron-donating and electron-absorbing groups mediocre degradation rates (0.1 min^{-1} < k_{obs} < 0.4 min^{-1}). The Co-SAC/PMS system showed similar degradation activities

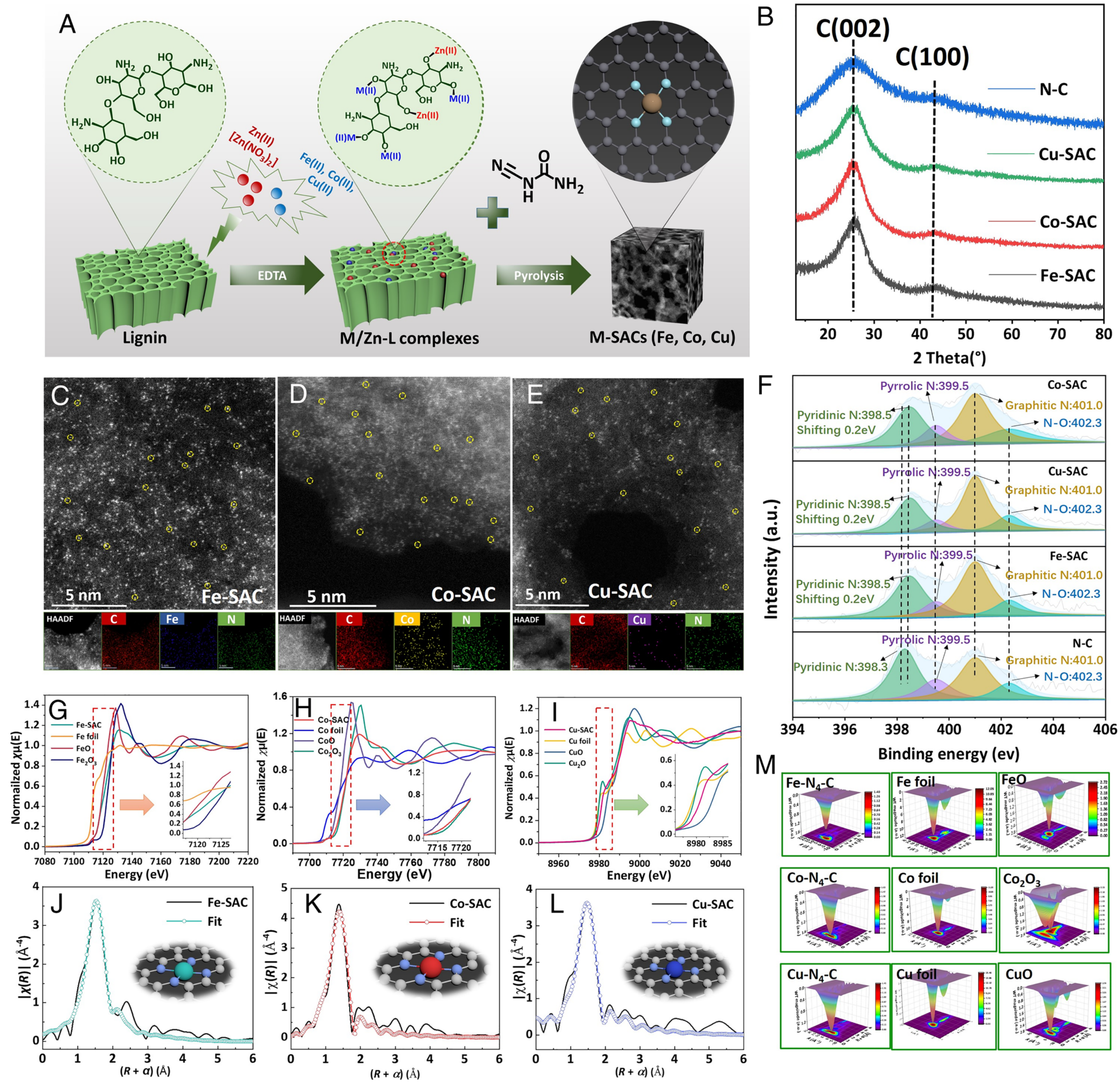

Fig. 1. (*A*) Preparation scheme of M-SACs (Fe-SAC, Co-SAC, and Cu-SAC) from lignin-based precursor; (*B*) XRD patterns of Fe-SAC, Co-SAC, and Cu-SAC; (*C–E*) HAADF-HRTEM image as well as the mappings of (*C*) Fe-SAC, (*D*) Co-SAC, and (*E*) Cu-SAC; (*F*) XPS N1s of the Fe-SAC, Co-SAC, Cu-SAC, and N-C catalysts; (*G–I*) XANES analysis of (*G*) Fe-SAC, (*H*) Co-SAC, and (*I*) Cu-SAC; (*J–L*) EXAFS of (*J*) Fe-SAC, (*K*) Co-SAC, and (*L*) Cu-SAC; (*M*) WT contour plots of Fe-SAC, Co-SAC, and Cu-SAC.

toward 16 representative pollutants as compared with those in the Fe-SAC/PMS system (Fig. 2*A*). The Cu-SAC also showed three degradation trends toward 16 representative pollutants but with lower degradation activity (Fig. 2*A*). Basically, the comparison of k_{obs} values with other SAC/PMS systems showed that Fe-SAC and Co-SAC exhibited extraordinary catalytic performances (Fig. 2*B* and *SI Appendix*, Table S4).

The $\varphi_{1/2}$ values of these pollutants were determined by the electrochemistry cyclic voltammetry (CV) analysis (*SI Appendix*, Fig. S9), which has been widely used to identify the redox potentials of various compounds (25, 28). Results showed in Fig. 2*C* indicated that the pollutants (e.g., PCM, BPA, CP, NPX, HBA, SN, SMZ, NP, CBZ, CTC, TC, CIP) with the $\varphi_{1/2}$ values lower than 1.2 V exhibited significant correlations ($R^2 = 0.841$) with their $\ln k_{obs}$ values in Fe-SAC. In contrast, NBA, NB, and CPL with very high $\varphi_{1/2}$ values exhibited low $\ln k_{obs}$, which were deviated from the correlated lines. Similar deviation between the $\varphi_{1/2}$ values of these pollutants and their $\ln k_{obs}$ values were also observed in the Co-SAC/PMS and Cu-SAC/PMS systems (Fig. 2*C*). Pollutants with $\varphi_{1/2}$ values lower than 1.2 V exhibited the characteristic that their rings are all directly attached with electron-donating groups (Fig. 2*A*, and Fig. 2*C*). This was also consistent with the results of Duan et al. (28), showing that the $\varphi_{1/2}$ values of various phenolic compounds had a good correlation with their $\ln k_{obs}$. In contrast, pollutants with rings attaching only electron-withdrawing groups showed very retarded anodic peak, and their $\varphi_{1/2}$ values were very high, indicating that these pollutants were difficult to be oxidized. As a result, using the $\varphi_{1/2}$ values could not represent all pollutants, especially for those with high $\varphi_{1/2}$ values. Other electronic parameters (i.e., electrophilic index,

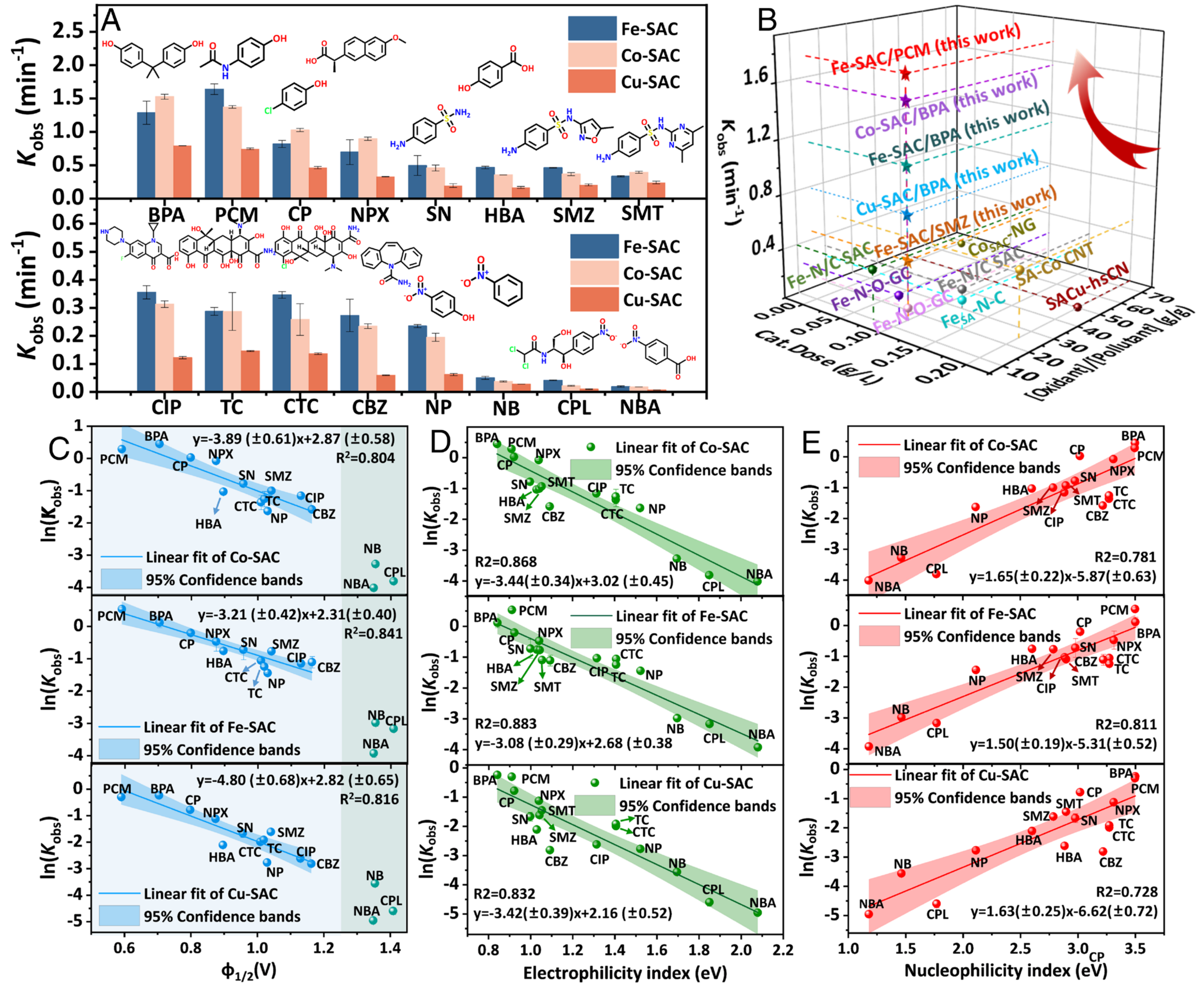

Fig. 2. (*A*) The k_{obs} values of different pollutants in M-SACs/PMS systems (concentrations of pollutants = 10 mg/L, $[Catalyst]_0$ = 0.1 g/L, $[PMS]_0$ = 0.5 mM, pH = 7.0). (*B*) Comparison of other SACs/PMS systems for pollutants oxidation. (*C*) Linearity between the $\varphi_{1/2}$ values of different pollutants and their $\ln k_{obs}$ values in M-SACs/PMS systems. (*D*) Linearity between the electrophilic indexes of different pollutants and their $\ln k_{obs}$ values in M-SACs/PMS systems. (*E*) Linearity between the nucleophilic indexes of different pollutants and their $\ln k_{obs}$ values in M-SACs/PMS systems.

nucleophilicity index, softness, hardness) of various pollutants were calculated via DFT analysis and shown in *SI Appendix*, Table S5. The electrophilic index, which reflects the ability of the pollutants to accept/donate electrons in the M-SACs/PMS systems (29, 30), correlates well with the $\ln k_{obs}$ values of the pollutants (R^2 = 0.832 to 0.883) in different M-SACs (Fe, Co and Cu)/PMS systems, including those with low k_{obs} values (Fig. 2*D*). For example, pollutants with lower electrophilic index (such as PCM, BPA, CP) exhibited lower electron-accepting ability and stronger electron-donating ability, which showed a higher $\ln k_{obs}$ value in all designed M-SACs/PMS systems. This was also confirmed by the nucleophilic index of the pollutants. The higher nucleophilicity index also reflected the stronger capacity of pollutants to donate electrons but lower capacity to accept electrons (29, 30), which showed a certain correlation (R^2 = 0.728 to 0.811) with their $\ln k_{obs}$ values but lower than that (R^2 = 0.832 to 0.883) of electrophilic index (Fig. 2 *D* and *E*). In contrast, other parameters, such as softness and hardness of pollutants, showed no correlations with the degradation of pollutants (*SI Appendix*, Fig. S10). As a result, the capacity of pollutants to donate/accept electrons (as measured by the electrophilic index) seemed to affect their degradation kinetics in SACs-based Fenton-like systems.

Analysis of Oxidation Pathways in M-SACs/PMS Systems. Adsorption of typical pollutants by the M-SACs was first evaluated, and the results showed that approximately 20 to 30% of pollutants (except for 60% of BPA adsorption) could be uptaken by the Fe-SAC (*SI Appendix*, Fig. S11), which might be due to the high surface area (122.0 m^2/g) of Fe-SAC with available adsorption sites for these pollutants (*SI Appendix*, Fig. S12 and Table S6). In addition, the Fe-SAC/PMS system maintained the outstanding oxidation capacity under different pH and with the presence of diverse anions and HA in the background, which indicated its strong anti-interference ability (*SI Appendix*, Fig. S13). As a result, the high degradation performance could be maintained in the real water matrixes (*SI Appendix*, Fig. S14). The degradation mechanisms of the Fe-SAC/PMS system toward 16 representative pollutants were determined via the quenching tests. TBA is a specific scavenger for $HO^{\bullet}$ due to its high reactivity with $\bullet OH$ ($k_{\bullet OH, TBA} = 7.6 \times 10^8$ $M^{-1}S^{-1}$) and the EtOH is a typical probe for both $SO_4^{\bullet-}$ and $\bullet OH$

with highly reactivity (31, 32). As shown in Fig. 3*A* and *SI Appendix*, Fig. S15, the addition of TBA and EtOH (100 mM) only showed a very small retarding effect on the oxidation of PCM and BPA. In contrast, the degradation of CBZ and NP was significantly decreased by adding the TBA and EtOH with k_{obs} reduction of 70 to 80%. EPR tests indicated that all M-SACs (Fe, Co, and Cu)/PMS could generate large amounts of radicals ($SO_4^{\bullet-}$ and •OH) and all pollutants could consume the radicals (Fig. 3*B* and *SI Appendix*, Fig. S16). Such a phenomenon indicated that radical oxidation occurred in all pollutant-oxidation systems, but the roles of radicals varied greatly depending on the target pollutants, which may be due to the different structural properties of different pollutants affecting their sensitivity to radical and nonradical oxidation.

The contributions of radicals and nonradical pathways for oxidating 16 representative pollutants in the M-SACs/PMS systems can be further identified via a premixture of M-SACs and PMS at designed time intervals before adding the pollutants (33, 34). Premixing the Fe-SAC and PMS for 3 and 6 min showed trival inhibition on the degradation of pollutants with lower electrophilic index, such as PCM, BPA, and CP (Fig. 3*C* and *SI Appendix*, Fig. S17), which indicated that the nonradical overwhelmed the effect of radicals in oxidating the pollutants with stronger electron-donating capacities. In contrast, the degradation of pollutants with higher electrophilic index (e.g., CBZ, CIP, and NP) showed a noticeable decay effect with the k_{obs} values decreasing more than 70% at the premixing time of 6 min (*SI Appendix*, Fig. S17). Since

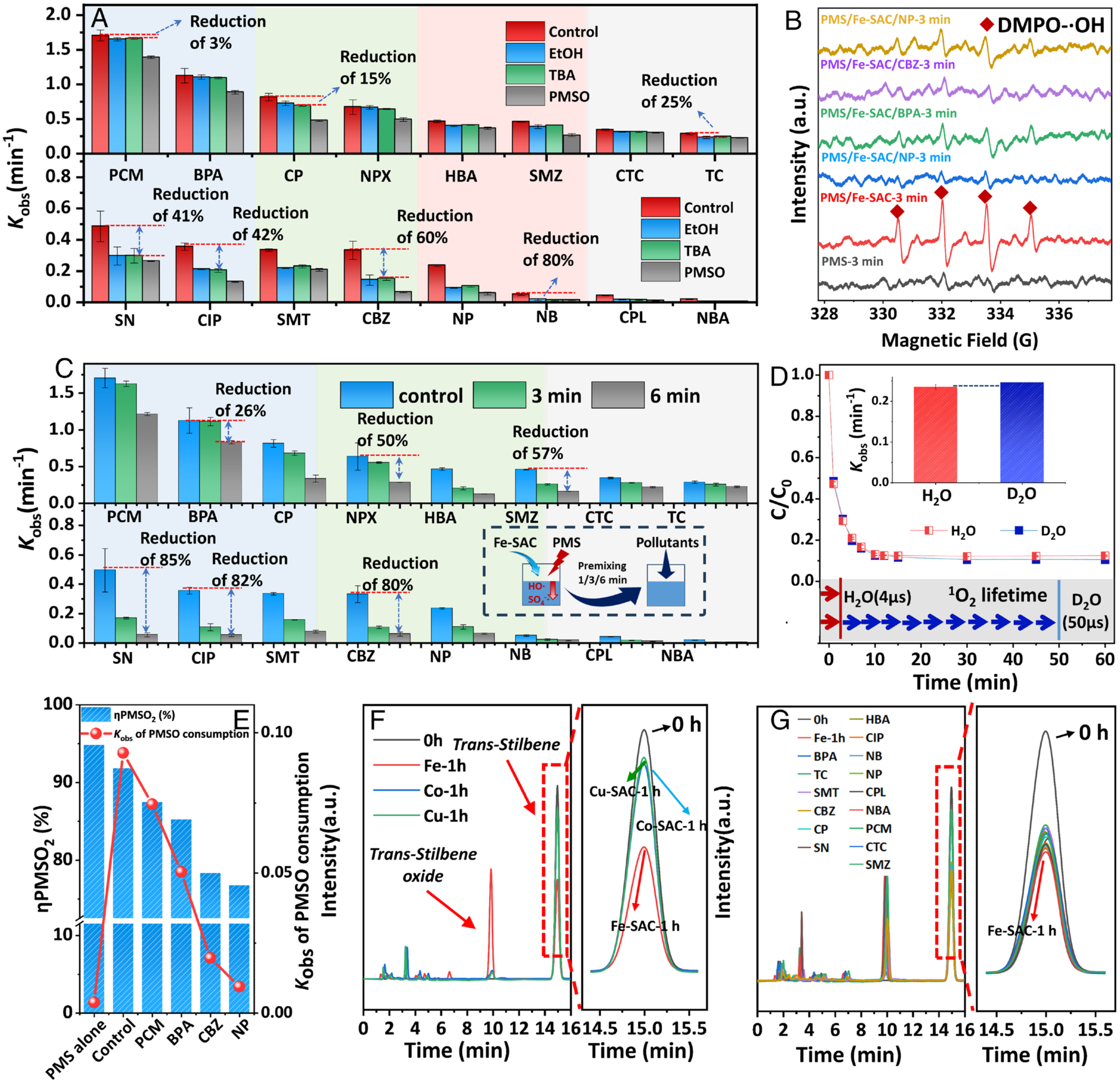

Fig. 3. (*A*) Retarding effect on the oxidation of different pollutants in the Fe-SAC/PMS system by adding TBA, EtOH, and PMSO. (*B*) DMPO-•OH signals in different Fe-SAC/PMS systems. (*C*) The k_{obs} values of premixing test at designed time intervals. (*D*) Degradation of pollutants in the Fe-SAC/PMS system with D_2O and H_2O as solutions. (*E*) The η_{PMSO2} and k_{obs} of PMSO consumption in the Fe-SAC/PMS system with/without the addition of pollutants. (*F*) The oxidation of trans-stilbene in M-SACs (Fe, Co, and Cu)/PMS systems. (*G*) Oxidation of trans-stilbene in the Fe-SAC/PMS system with/without the addition of pollutants (concentrations of pollutants = 10 mg/L, 80% acetonitrile; trans-stilbene: 1.0 mM; $[Catalyst]_0$ = 0.1 g/L, $[PMS]_0$ = 0.5 mM, pH = 7.0).

radicals were continuously consumed during the premixture of Fe-SAC and PMS, the density of radicals that can participate in the degradation reaction was greatly reduced. This result indicated that free radicals played a more important role in the oxidation of pollutants with a higher electrophilic index. As a result, the role of other nonradical oxidation pathways [e.g., singlet oxygen ($^1O_2$), high-valent iron-oxo species, electron transfer process (ETP)] triggered in the Fe-SAC/PMS system should be further identified (11, 24, 35–38).

As for the $^1O_2$, since the lifetime of $^1O_2$ in D_2O was 10 times higher than that in H_2O, the role of $^1O_2$ can be excluded via using D_2O as solution (22, 25, 38), which showed similar k_{obs} value by comparing with that in H_2O (Fig. 3*D*). This was also confirmed by the EPR spectra for $^1O_2$ signals in different M-SACs (Fe-SAC, Co-SAC, and Cu-SAC)/PMS systems, which showed very weak $^1O_2$ signals with/without the addition of pollutants (*SI Appendix*, Figs. S16 and S18). The high-valent iron-oxo oxidation in the Fe-SAC/PMS system was evaluated by using PMSO as a scavenger, which showed strong inhibitory effect toward CBZ and NP but little inhibition of PCM and BPA (Fig. 3*A*). The results suggested that high-valent iron-oxo exerted better contribution toward NP and CBZ degradation; this was also consistent with the results of Xing's groups, unveiling that high-valent iron-oxo demonstrated a greater role for oxidizing the pollutants with higher half-wave potential (3). However, the high-valent iron-oxo oxidation toward different pollutants cannot be fully explained via quenching results since two oxidation pathways of PMSO occurred in the Fe-SAC/PMS system, including i) the oxidaiton of PMSO into hydroxylated PMSO/biphenyl compounds via the radical pathways and ii) conversion of PMSO into $PMSO_2$ by the high-valent metal-oxo oxidation (39–41). The yield of $PMSO_2$ (η_{PMSO2}) was calculated via the ratio of $PMSO_2$ production and PMSO consumption to further evaluate the role of high-valent iron-oxo species (42). The results showed the η_{PMSO2} values in the Fe-SAC/PMS system also depended on the targeted pollutants (Fig. 3*E* and *SI Appendix*, Fig. S19). Although the η_{PMSO2} of PMS alone was more than 90%, k_{obs} of PMSO consumption was very low. In contrast, PMSO consumption was quickly increased to 0.091 min^{-1} in the Fe-SAC/PMS system with more than 90% of η_{PMSO2}, and it was decreased with the addition of pollutants; this result indicated that high-valent iron-oxo was generated in the Fe-SAC/PMS system (43, 44). The decreased η_{PMSO2} and k_{obs} of PMSO consumption by the addition of pollutants might be due to that other oxidation pathways were principally triggered toward the targeted pollutants in the Fe-SAC/PMS system with the inhibition on the consumption of PMSO and generation of high-valent iron-oxo species (25). The existence of high-valent iron-oxo oxidation in the Fe-SAC/PMS system can be confirmed by the oxidation of trans-stilbene toward trans-stilbene oxide (3), as shown in Fig. 3*F*. The high-valent cobalt-oxo and high-valent copper-oxo species were almost excluded in Co-SAC/PMS and Cu-SAC/PMS systems based on the unfavorable oxidation of trans-stilbene (Fig. 3*F*). The roles of high-valent metal-oxo oxidation toward 16 representative pollutants were further identified in the Fe-SAC/PMS system. Results showed that the addition of 16 representative pollutants only showed a very small increase in the trans-stilbene peak (Fig. 3*G*). This result indicated that the addition of pollutants only shared a very small fraction of high-valent iron-oxo oxidation. As a result, although high-valent iron-oxo oxidation existed in the Fe-SAC/PMS system, its role was very weak for the degradation of these pollutants.

Electrochemical Analysis of ETP. It was reported that the open-circuit potentials could intuitively reflect whether electron transfer occurred in catalytic systems or participated in the oxidation of pollutants (28, 45, 46). The open-circuit potentials of different M-SACs electrodes remarkably increased after the addition of PMS due to the formation of substable M-SACs/PMS complexes that facilitated the potential of M-SACs electrodes (*SI Appendix*, Fig. S20). The potentials of Fe-SAC/PMS complexes and Co-SAC/PMS complexes were quite similar, while they were significantly higher than that of the Cu-SAC/PMS complexes. This might be due to that the binding ability of Cu atom with PMS was smaller than those of the Co and Fe atoms (22, 47). To further identify the versatile roles of pollutants on the ETP oxidation, different pollutants were added into the electrochemical Fe-SAC/PMS systems, which showed significantly different falling potential trends (Fig. 4 *A* and *B* and *SI Appendix*, Fig. S21). The decrease in the open-circuit potential after adding pollutants was due to the electron-donating from the pollutants to the Fe-SAC/PMS complexes, resulting in the decomposition of surface complex (20, 25, 48). As a result, different ETP oxidation trends toward the pollutants with different electrophilic indexes (reflecting the electron-donating capacity of the pollutants) would occur in the Fe-SAC/PMS system, with PMS as electron acceptor and pollutants as electron donor. This result can be confirmed by the linear correlation between the k_{obs} obtained in different pollutants systems and their falling potentials, which showed the correlation of R^2 = 0.939 (Fig. 4*C*). The ETP regime in the Fe-SAC/PMS system could be further unveiled by the Amperometric i-t curve via regulating the addition sequence of PMS and pollutants (*SI Appendix*, Figs. S22–S24 and *Text S2*), which indicated the binding of PMS with Fe-SAC to form the Fe-SAC/PMS complex was the prerequisite to initate ETP oxidation, followed by the electron transfer from pollutant molecules to the Fe-SAC/PMS complex.

A galvanic oxidation system (GOS) was developed to reveal the ETP between the pollutants and metastable M-SACs/PMS complexes considering that the electrons can transfer from the molecules of pollutants to M-SAC/PMS complexes via an electron channel if ETP occurred in the M-SACs/PMS systems (49, 50). The three M-SACs were deposited onto the graphite electrode (superficial area of 27.2 cm^2), and the oxidant (PMS) and pollutant were added into two separated cells via the connection of the agar salt bridge and an Ampere meter (Fig. 4*D*). As showed in Fig. 4*E* and *SI Appendix*, Fig. S25, the GOS systems loading with Fe-SAC and Co-SAC exhibited the similar current (453.0 to 476.3 μA) by adding PCM as the probe pollutant, followed by Cu-SAC with current of 239.1 μA (GOS with bare graphite electrode showed very low current). This result further confirmed the stronger electron transfer in the Co-SAC/PMS and Fe-SAC/PMS systems. In addition, the effect of different pollutants on the current change was determined in the Fe-SAC-based GOS system (Fig. 4*F*), and PCM exhibited the highest current (453.0 μA), which was followed by the addition of BPA (274.6 μA), CBZ (151.2 μA), and NP (95.2 μA). As a result, the pollutants (e.g., PCM, and BPA) with lower electrophilic index can trigger higher ETP via the electron-donating from the pollutant molecules to Fe-SAC/PMS complexes. Basically, the contributions of radical and nonradical pathways (mainly based on ETP oxidation) toward 16 representative pollutants in M-SACs/PMS systems (Fe-SAC as example) were calculated (Fig. 4*G*), and high distributing proportions of ETP oxidation (>97%) toward PCM and BPA can be due to the low electrophilic indexes of these targeted pollutants with strong electron donating to the Fe-SAC/PMS complexes.

DFT Calculation. The universal of the comediated ETP oxidation by pollutants and M-SACs was further identified by the DFT calculation via the molecular orbital (MO) analysis of M-SACs (Fe, Co, and Cu)/PMS complexes and 16 representative

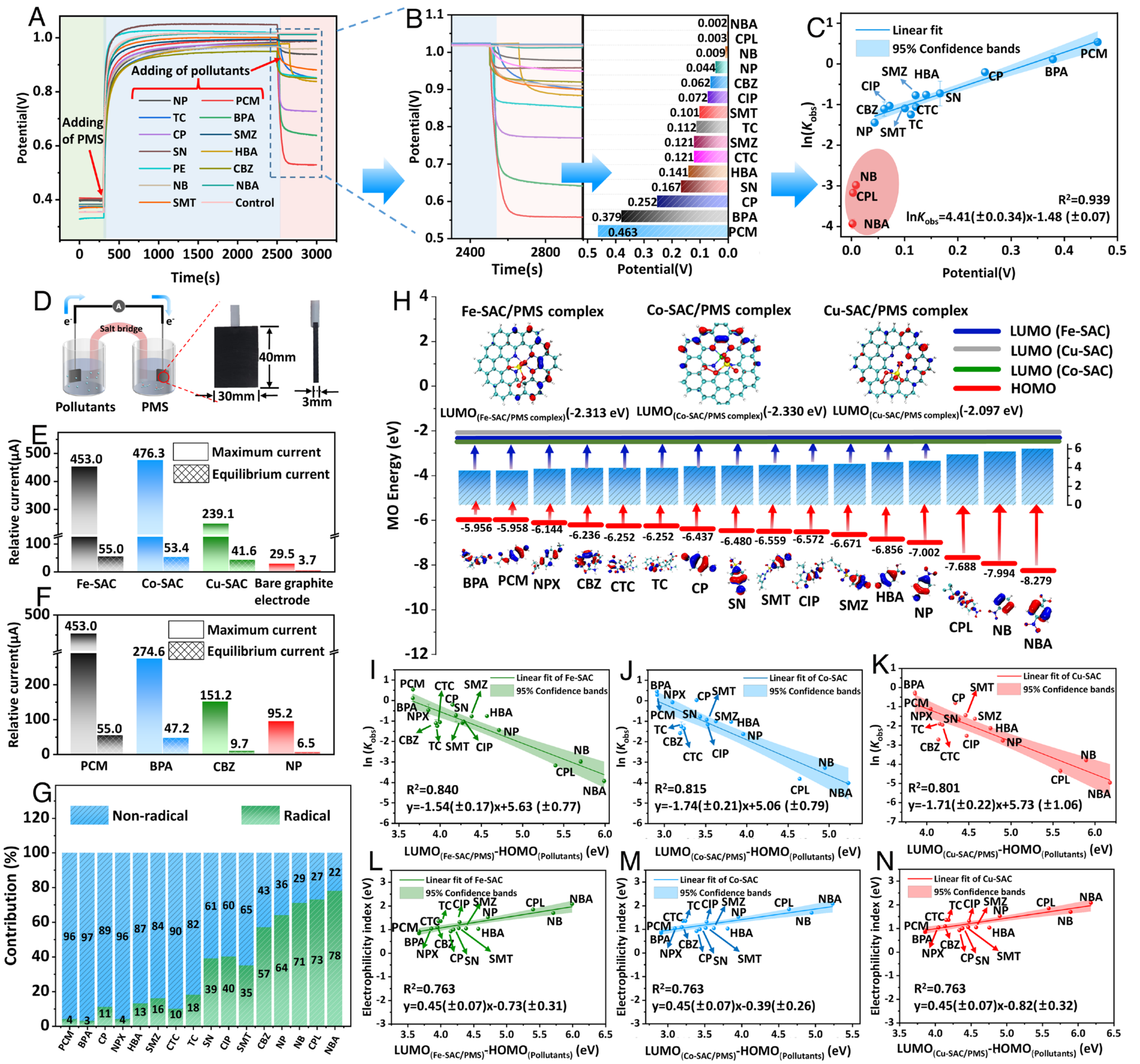

Fig. 4. (*A*) Open-circuit potential of the Fe-SAC electrode after adding PMS and different pollutants. (*B*) Different falling potentials after adding different pollutants. (*C*) Correlation between the k_{obs} of different pollutants obtained in Fe-SAC/PMS systems and their falling potentials. (*D*) Scheme of GOS depositing with M-SACs. (*E*) Currents after adding PCM in different GOS systems depositing with Fe-SAC, Co-SAC, and Cu-SAC. (*F*) Currents after adding different pollutants in the Fe-SAC-based GOS system. (*G*) Contributions of radical and nonradical pathways toward the degradation of different pollutants in Fe-SAC/PMS systems. (*H*) Different energy gaps between different $\text{LUMO}_{(\text{M-SACs/PMS complexes})}$ and $\text{HOMO}_{\text{pollutants}}$. (*I*–*K*) Correction between the calculated gaps and $\ln k_{obs}$ of pollutants obtained in the (*I*) Fe-SAC/PMS system, (*J*) Co-SAC/PMS system, and (*K*) Cu-SAC/PMS system. (*L*–*N*) Correction between the calculated gaps and electrophilic indexes of pollutants in the (*L*) Fe-SAC/PMS system, (*M*) Co-SAC/PMS system, and (*N*) Cu-SAC/PMS system.

pollutants (51, 52). The premise of ETP oxidation in M-SACs/PMS systems was based on the electron transfer from the Highest Occupied Molecular Orbital (HOMO) of pollutants (*SI Appendix*, Fig. S26) to Lowest Unoccupied Molecular Orbital (LUMO) of M-SACs/PMS complexes (25, 28, 53). As shown in the Fig. 4*H* and *SI Appendix*, Fig. S27, the LUMO (−2.097 eV) of Cu-SAC/PMS complexes was less negative as compared with those (−2.313 to −2.330 eV) of Fe-SAC/PMS complexes and Co-SAC/PMS complexes, which mean that a greater energy gap would be required for electron donating from the pollutants to the Cu-SAC/PMS complexes (25, 54, 55). A lower gap between $\text{LUMO}_{(\text{M-SACs/PMS complexes})}$ and $\text{HOMO}_{\text{pollutants}}$ represented that the electrons migration can be more easily triggered from the pollutants to the M-SACs/PMS complexes (25, 54, 55), thus accelerating the ETP oxidation toward the targeted pollutants. This result explained the relatively slower ETP oxidation in the Cu-SAC/PMS system. The Fe-SAC/PMS complexes and Co-SAC/PMS complexes showed similar LUMO values (−2.313 and −2.330 eV). These results are in consistent with the degradation performances in M-SACs/PMS systems, where ETP attained similar oxidation capacities toward targeted pollutants with low electrophilic indexes.

In addition, the energy gaps between the LUMO of M-SACs/PMS complexes ($\text{LUMO}_{(\text{M-SACs/PMS complexes})}$) and the HOMO of different pollutants ($\text{HOMO}_{\text{pollutants}}$) were calculated. The calculated gaps also showed well corrections with the $\ln k_{obs}$ data (R^2 = 0.801 to

840) obtained in the respective M-SACs/PMS systems (Fig. 4 *I–K*) and electrophilic indexes ($R^2 = 0.763$) of different pollutants (Fig. 4 *L–N*). As a result, ETP oxidation would be more prone to the degradation of pollutants (e.g., BPA, PCM) with lower electrophilic indexes, overwhelming the role of radical oxidation in the M-SACs/PMS systems. In contrast, the higher electrophilic indexes of pollutants represented the weaker electron-donating capacity causing the higher gaps between the $\mathrm{LUMO}_{\text{(M-SACs/PMS complexes)}}$ and $\mathrm{HOMO}_{\text{pollutants}}$, which resulted in the weaker ETP oxidation accompanying with noticeable radical oxidation. In addition, the ETP oxidation in different M-SACs/PMS systems can be regulated via the energy gaps between the different M-SACs/PMS complexes and pollutants. For example, the weaker ETP in the Cu-SAC/PMS system was due to the greater energy gap required for electron donating from the pollutants to the Cu-SAC/PMS complexes (Fig. 4*H*). As a result, the Fenton-like efficiencies and pathways in the M-SACs/PMS systems could be well modulated by the tunable ETP oxidation, which was collectively determined by the M-SACs and pollutants.

Continuous Oxidation System. The Fe-SAC showed excellent performance for various oxidation, and it was also more environmentally friendly and less toxic as compared with Co-SAC; this encouraged us to further realize the device integration of Fe-SAC for water purification (56, 57). Ceramic membrane (CM) has the advantages of oxidation resistance, high mechanical strength, good chemical stability, etc., which can be used as an excellent catalytic membrane carrier. A water-purification membrane was fabricated by fixing the Fe-SAC on the CMs (25 cm × 10 cm) via a spraying-cross-linking method (Fig. 5*A* and *SI Appendix*, Figs. S28 and S29). The scanning electron microscopy (SEM) image of Fe-SAC/CMs showed that Fe-SAC was deposited on the surface of CMs (*SI Appendix*, Fig. S30), which provided sufficient active sites for rapid degradation of pollutants in contaminated water. Cross-section SEM image of the Fe-SAC/CMs as well as their element mappings further exhibited the deposited Fe-SAC layer with a thickness of ~110 µm (Fig. 5 *B* and *C*). The contact angle tests can reflect the change of hydrophilicity before and after the loading of catalyst on the surface of CMs (20). Results showed that the Fe-SAC/CMs exhibited a similar hydrophilicity property as compared with that of bare CM (*SI Appendix*, Fig. S31). Benefiting from its superior hydrophilicity, the Fe-SAC/CMs only showed a steady decrease in water flux from 170 to 152 L m^{-2} h^{-1} although a steady thickness of Fe-SAC was deposited on the CMs surface, partially blocking the pores of CMs (Fig. 5*D*). As a result, the high and stable water flux of Fe-SAC/CMs would be beneficial to the continuous water purification.

The degradation performances of typical pollutants (e.g., PCM, BPA, NP, CBZ) in the Fe-SAC/CMs was evaluated by compared with that in bare CMs. Results showed that the complete oxidation of a series of pollutants in a continuous flow can be achieved in the Fe-SAC/CMs, while the bare CMs could only remove 7.2 to 34.2% of pollutants (Fig. 5*E*). The Fe-SAC/CMs were also used for the removal of pollutants in wastewater secondary effluent (Fig. 5*F*). Results showed that multiple pollutants at environmental conditions could be well removed by Fe-SAC/CMs via PMS activation. In

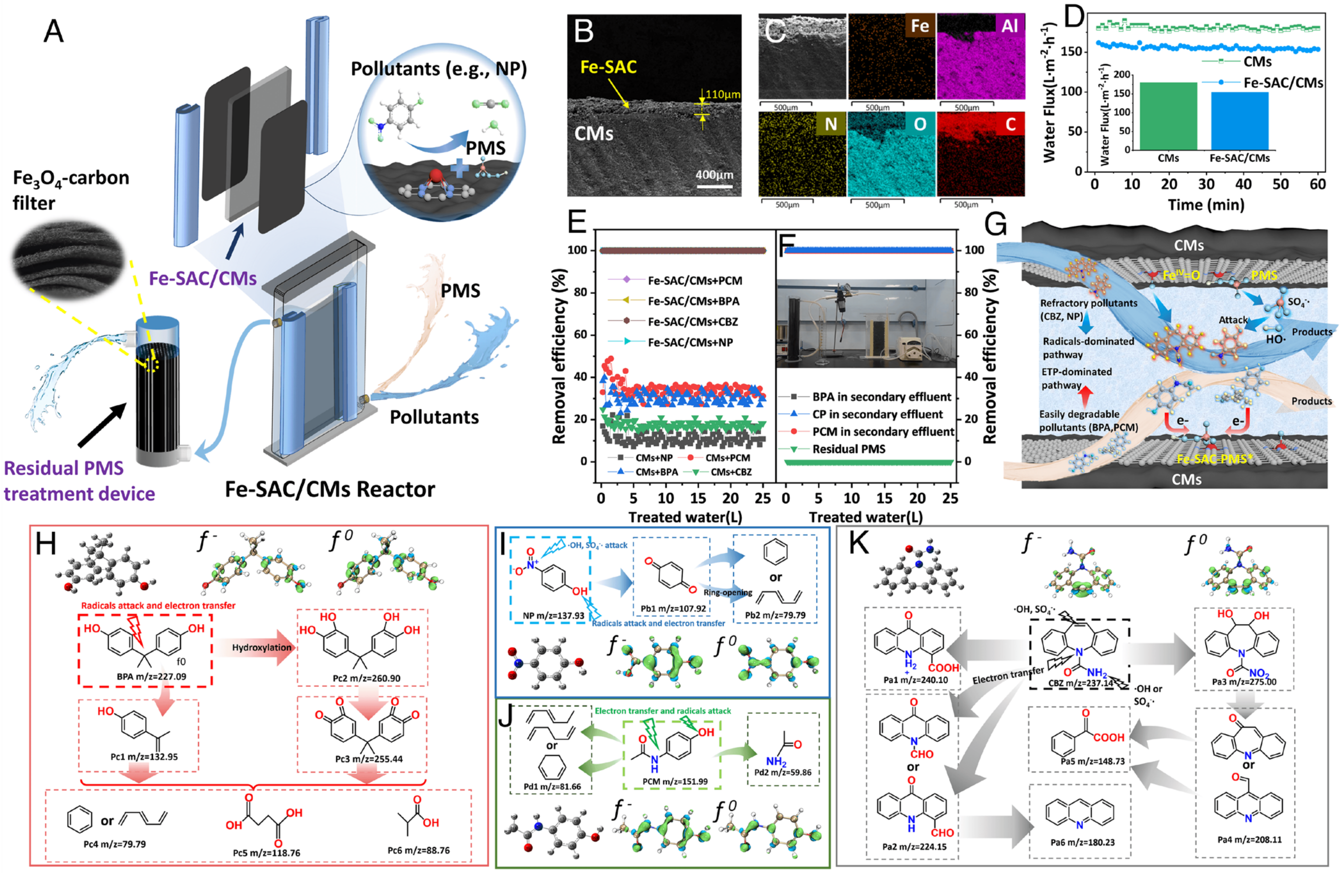

Fig. 5. (*A*) Scheme of Fe-SAC/CMs for continuous water purification. (*B*) Cross-section SEM of Fe-SAC/CMs and (*C*) element mappings. (*D*) Water flux of bare CMs and Fe-SAC/CMs. (*E*) Degradation performances of typical pollutants in the continuous Fe-SAC/CMs system. (*F*) Degradation performances of multiple pollutants from wastewater secondary effluent by the Fe-SAC/CMs. (*G*) Scheme of the continuous Fe-SAC/CMs system toward pollutant oxidation. (*H–K*) Fukui functions as well as degradation pathways of (*H*) BPA, (*I*) NP, (*J*) PCM, and (*K*) CBZ.

addition, a device (inner diameter of 8 cm, length of 30 cm) filled with Fe_3O_4-loaded felt was designed for subsequent processing of PMS (*SI Appendix*, Fig. S29), which could effectively consume the residual PMS in the effluent (Fig. 5*F*). Basically, the Fe-SAC/PMS systems could trigger a series of oxidation pathways (e.g., radicals, high-valent iron-oxo oxidation, and ETP) toward these pollutants, which guaranteed the high effective and stable degradation activity in the Fe-SAC/CMs (Fig. 5*G*).

The intermediate products of 16 representative pollutants were identified and their degradation pathways were diagramed (Fig. 5 *H*–*K* and *SI Appendix*, Figs. S32–S47). Since the electron-donating groups can be easily oxidized by various nonradical pathways (e.g., $^1O_2$, high-valent metal-oxo, ETP), the electron-donating groups (e.g., hydroxyl, and amido groups) of pollutants (e.g., BPA, PCM) can be easily cleaved by the enhanced nonradical pathways (ETP dominated) in the Fe-SAC/PMS systems. In addition, the cleavage of electron-withdrawing groups can also be observed in the pollutants and their intermediates, which were inert to be oxidized by the nonradical electrophilic pathway. For example, the NP and its intermediates with electron-withdrawing C=O groups and nitro group can be well decomposed due to the large amounts of •OH and $SO_4^{\bullet -}$ in the Fe-SAC/PMS system, followed by the opens of benzene ring via ETP oxidation (Fig. 5*I*). The reactive sites of these pollutants could also be evaluated by the Fukui function representing electrophilic attack (f^-) and radical attack (f^0). As depicted in Fig. 5*H*, the f^- and f^0 regions for BPA were distributed over the whole molecule, suggesting both the nonradical electrophilic attack and radical attack would occur at these positions. The f^- region for NP mainly located at the hydroxyl groups and C1, C2, C5, and C6 of the benzene ring, while the f^0 regions of NP showed a difference to f^- where the radical attack become feasible at both nitro and hydroxyl groups (Fig. 5*I*). Distributions of electrostatic potential of NP configuration showed the high electronegativity of nitro groups as well as the high electropositivity of benzene ring and hydroxyl groups (*SI Appendix*, Fig. S48), which corresponded to the reactive sites of NP for mostly like radical attack and electrophilic attack. This was consistent with the Fukui function of NP and its degradation pathways. The Fukui functions and electrostatic potential of other pollutants corresponding to their degradation pathways were shown in *SI Appendix*, Figs. S47 and S48. Since the Fe-SAC/PMS system could promote both radical and ETP oxidation, versatile dominating degradation pathways toward different pollutants can be controlled by modulated ETP oxidation via the synergy of Fe-SAC and pollutants.

Conclusions

The relationship between the specific properties of pollutants and the oxidation activities/pathways toward different pollutants in SACs/PMS systems was still ambiguous. In this study, various oxidation activities and oxidation pathways to target pollutants in M-SACs/PMS systems were systematically explained from the perspective of pollutant characteristics. Sixteen representative pollutants showed different electrophilic indexes, which were correlated well (R^2 = 0.832 to 0.883) with their $\ln k_{obs}$ values in versatile M-SACs (Fe, Co, and Cu)/PMS systems. In addition, different energy gaps between the M-SACs/PMS complexes and pollutants can be obtained by the DFT calculations, which represented the electrons migration capacity from the pollutants to the M-SACs/PMS complexes. Results showed that calculated gaps exhibited well correlations with $\ln k_{obs}$ data (R^2 = 0.801 to 840) obtained in the respective M-SACs/PMS systems and electrophilic indexes (R^2 = 0.763) of different pollutants, which evidenced the universality of tunable ETP oxidation in M-SACs/PMS systems. As a result, the Fenton-like efficiencies and pathways in the M-SACs/PMS systems could be well modulated by the tunable ETP oxidation, and the ETP oxidation in these M-SACs/PMS systems be collectively determined via the synergy of M-SACs and pollutants. In addition, a membrane catalytic system was fabricated via depositing the Fe-SAC onto CMs, which exhibited continuous and high effective degradation activity toward various micropollutants. Based on insights from this work, we reveal Fenton-like systems with regulated oxidation processes from the perspective of comodulation of pollutants and SACs-induced ETP.

Materials and Methods

Chemicals and Reagents. The chemicals, including alkali lignin, $KHSO_5 \cdot 0.5KHSO_4 \cdot 0.5\ K_2SO_4$ (PMS), dicyandiamide, $Zn(NO_3)_2 \cdot 6H_2O$, N, N-Diethyl-p-phenylenediamine sulfate salt, $FeCl_2$, $CoCl_2$, CuCl, Na_2SO_4, N, N-dimethylformamide, 5,5-dimethylpyrroline-oxide (DMPO), ethanol (EtOH), tert-butyl alcohol (TBA), Nafion perfluorinated resin, and trans-stilbene, were obtained from Sinopharm Chemical Reagent Co. Ltd. Sixteen kinds of targeted pollutants were used in this study, including paracetamol (PCM), bisphenol A (BPA), p-chlorophenol (CP), naproxen (NPX), hydroxybenzoic acid (HBA), carbamazepine (CBZ), ciprofloxacin (CIP), chlorotetracycline (CTC), nitrobenzene (NB), tetracycline (TC), sulfamethazine (SMT), sulfanilamide (SA), sulfamethoxazole (SMZ), p-nitrophenol (NP), chloramphenicol (CPL), and p-nithbenzoic acid (NBA), which were obtained from Aladdin Co. Ltd. The ceramic membrane (10 cm × 25 cm) was purchased from Suzhou Environmental Technology Co. Ltd. The wastewater secondary effluent was collected from the second sedimentation tank effluent of Green Ring sewage treatment plant in Gaoqing County, Zibo City, Shandong Province.

Catalysts Preparation. The M-SACs catalysts were fabricated via one-step pyrolysis of lignin-based precursor. As for the Fe-SAC, the alkali lignin (4.0 g), $FeCl_2$ (28 mmol), and $Zn(NO_3)_2 \cdot 6H_2O$ (28 mmol) were mixed with the deionized water (500 mL), stirred, and stood for 12 h to form the Fe/Zn-lignin complexes. It was then followed by the vacuum filtration to collect the Fe/Zn-lignin complexes from the mixture. The complexes were dried for 24 h at 60 °C, ground into powers, and mixed with 10 times the weight of dicyandiamide. Finally, the mixture was put into a quartz boat, pyrolyzing in a tubular furnace under N_2 atmosphere at 550 °C for 1 h and 950 °C for another 1 h. The fabrication of Co-SAC and Cu-SAC followed the same procedures by replacing the $FeCl_2$ with $CoCl_2$ and $CuCl_2$, respectively.

The fabrication of Fe-SAC/CM includes three steps. i) The Fe-SAC (1.0 g) was first mixed with 60 mL of PVA solution (5 mg/mL) and the mixture was ultrasonically dispersed for 0.5 h. ii) Thereafter, the ink of Fe-SAC was evenly sprayed on the front and rear surface of CM (10 cm × 25 cm) by using the airbrush (Hansa Infinity, Germany). iii) The Fe-SAC deposited CM was then immersed into the succinic acid solution (1.0 wt.%) for 2 h, dried at 60 °C in a vacuum oven for 8 h, and then heated at 250 °C to remove residual agents.

Characterization Methods. The XAS spectra of M-SACs were measured by the Shanghai Synchrotron Radiation Facility (SSRF), China, which were performed with an electron energy of 3 GeV. The radiation was monochromatized by a Si (111) double-crystal monochromator. XANES and EXAFS data reduction and analysis were processed by Athena software. The HAADF-STEM images were recorded with an FEI Themis Z scanning transmission electron microscope with double aberration correctors in STEM mode. Metal contents in the M-SACs were measured by inductively coupled plasma mass spectrometry (Agilent 720ES). The surface morphologies of the catalyst as well as the catalytic membrane were measured by a field-emission scanning electron microscope (FE-SEM, Hitachi, SU8010) at 5 kV. The surface elements in the catalysts were characterized by the XPS analysis (Thermo Scientific K-Alpha). The crystal structure was determined by powder XRD with a Rigaku Smartlab X-ray diffractometer.

Experiment Procedures. The M-SACs catalyst (0.1 g/L) was added to the solution containing the design concentration of pollutants, and then, a certain concentration of PMS was added. At a certain time interval, 1 mL of samples was taken and filtered through a nylon membrane (0.22 μm). The sample was quickly mixed with 20 μL of sodium thiosulfate to quench the reaction. All experiments were repeated two to three times in 100 mL of conical flasks to ensure reproducibility. Detection details of pollutants and radicals were supplemented in *SI Appendix*, *Text S1*. The detection conditions for all pollutants were given in *SI Appendix*, Table S7. All electrochemical analysis and the detection of $\varphi_{1/2}$ values were given in *SI Appendix*, *Text S2*.

Computational Methods. The spin-polarized DFT calculations were carried out with the Vienna Ab initio Simulation Package within the generalized gradient approximation using the Perdew–Burke–Ernzerhof functional. More details about the DFT calculations are provided in *SI Appendix*, *Text S3*.

Data, Materials, and Software Availability. All study data are included in the article and/or *SI Appendix*.

ACKNOWLEDGMENTS. The work was supported by the National Natural Science Foundation of China (52170086), Natural Science Foundation of Shandong Province (ZR2021ME013), and Shandong Provincial Excellent Youth (ZR2022YQ47). We want to thank Conghua Qi from Shiyanjia Lab (https://www.shiyanjia.com) for XAFS analysis.

Author affiliations: [a]Shandong Key Laboratory of Water Pollution Control and Resource Reuse, School of Environmental Science and Engineering, Shandong University, Qingdao 266237, People's Republic of China; [b]College of Safety and Environmental Engineering, Shandong University of Science and Technology, Qingdao 266590, People's Republic of China; [c]Environment Research Institute, Shandong University, Qingdao 266237, People's Republic of China; and [d]School of Chemical Engineering, The University of Adelaide, Adelaide, SA 5005, Australia

1. M. A. Shannon *et al.*, Science and technology for water purification in the coming decades. *Nature* **452**, 301–310 (2008).
2. Z. Y. Guo *et al.*, Electron delocalization triggers nonradical Fenton-like catalysis over spinel oxides. *Proc. Natl. Acad. Sci. U.S.A.* **119**, e2201607119 (2022).
3. C. Cheng *et al.*, Generation of Fe^{IV}=O and its contribution to Fenton-like reactions on a single-atom iron−N−C catalyst. *Angew. Chem. Int. Ed. Engl.* **62**, e202218510 (2023).
4. C. H. Gu *et al.*, Slow-release synthesis of Cu single-atom catalysts with the optimized geometric structure and density of state distribution for Fenton-like catalysis. *Proc. Natl. Acad. Sci. U.S.A.* **120**, e2311585120 (2023).
5. D. N. Pei, C. Liu, A. Y. Zhang, X. Q. Pan, H. Q. Yu, In situ organic Fenton-like catalysis triggered by anodic polymeric intermediates for electrochemical water purification. *Proc. Natl. Acad. Sci. U.S.A.* **117**, 30966–30972 (2020).
6. Q. Y. Wu, Z. W. Yang, Z. W. Wang, W. L. Wang, Oxygen doping of cobalt-single-atom coordination enhances peroxymonosulfate activation and high-valent cobalt–oxo species formation. *Proc. Natl. Acad. Sci. U.S.A.* **120**, e2219923120 (2023).
7. K. J. Rivenbark, M. Wang, K. Lilly, P. Tamamis, T. D. Phillips, Development and characterization of chlorophyll-amended montmorillonite clays for the adsorption and detoxification of benzene. *Water. Res.* **221**, 118788 (2022).
8. L. Wang *et al.*, Proton transfer triggered in-situ construction of C=N active site to activate PMS for efficient autocatalytic degradation of low-carbon fatty amine. *Water. Res.* **240**, 120119 (2023).
9. Y. Wang *et al.*, Natural polyphenols enhanced the Cu(II)/peroxymonosulfate (PMS) oxidation: The contribution of Cu(III) and HO•. *Water. Res.* **186**, 116326 (2020).
10. L. Peng, X. Duan, Y. Shang, B. Gao, X. Xu, Engineered carbon supported single iron atom sites and iron clusters from Fe-rich Enteromorpha for Fenton-like reactions via nonradical pathways. *Appl. Catal. B Environ.* **287**, 119963 (2021).
11. B. Wang *et al.*, A site distance effect induced by reactant molecule matchup in single-atom catalysts for Fenton-like reactions. *Angew. Chem. Int. Ed. Engl.* **61**, e202207268 (2022).
12. Y. Xiong *et al.*, Single-atom Fe catalysts for Fenton-Like reactions: Roles of different N species. *Adv. Mater.* **34**, 2110653 (2022).
13. M. Huang *et al.*, Facilely tuning the intrinsic catalytic sites of the spinel oxide for peroxymonosulfate activation: From fundamental investigation to pilot-scale demonstration. *Proc. Natl. Acad. Sci. U.S.A.* **119**, e2202682119 (2022).
14. Q. Zhou *et al.*, Generating dual-active species by triple-atom sites through peroxymonosulfate activation for treating micropollutants in complex water. *Proc. Natl. Acad. Sci. U.S.A.* **120**, e2300085120 (2023).
15. X. Liang *et al.*, Coordination number dependent catalytic activity of single-atom cobalt catalysts for fenton-like reaction. *Adv. Funct. Mater.* **32**, 2203001 (2022).
16. K. Yin *et al.*, Microenvironment modulation of cobalt single-atom catalysts for boosting both radical oxidation and electron-transfer process in Fenton-like system. *Appl. Catal. B Environ.* **329**, 122558 (2023).
17. Y. Shang, Y. Kan, X. Xu, Stability and regeneration of metal catalytic sites with different sizes in Fenton-like system. *Chin. Chem. Lett.* **34**, 108278 (2023).
18. F. Mo *et al.*, The optimized Fenton-like activity of Fe single-atom sites by Fe atomic clusters–mediated electronic configuration modulation. *Proc. Natl. Acad. Sci. U.S.A.* **120**, e2300281120 (2023).
19. Y. Qi *et al.*, Novel lignin-based single atom catalysts as peroxymonosulfate activator for pollutants degradation: Role of single cobalt and electron transfer pathway. *Appl. Catal. B Environ.* **286**, 119910 (2021).
20. K. Yin *et al.*, High-loading of well dispersed single-atom catalysts derived from Fe-rich marine algae for boosting Fenton-like reaction: Role identification of iron center and catalytic mechanisms. *Appl. Catal. B Environ.* **336**, 122951 (2023).
21. Z. Chen *et al.*, Single-atom Mo–Co catalyst with low biotoxicity for sustainable degradation of high-ionization-potential organic pollutants. *Proc. Natl. Acad. Sci. U.S.A.* **120**, e2305933120 (2023).
22. Y. Shang, X. Xu, B. Gao, S. Wang, X. Duan, Single-atom catalysis in advanced oxidation processes for environmental remediation. *Chem. Soc. Rev.* **50**, 5281–5322 (2021).
23. X. Mi *et al.*, Almost 100 % peroxymonosulfate conversion to singlet oxygen on single-atom CoN$_{2+2}$ sites. *Angew. Chem. Int. Ed. Engl.* **60**, 4588–4593 (2021).
24. Z. Zhao *et al.*, Turning the inert element zinc into an active single-atom catalyst for efficient Fenton-like chemistry. *Angew. Chem. Int. Ed. Engl.* **62**, e202219178 (2023).
25. M. Yang *et al.*, Unveiling the origins of selective oxidation in single-atom catalysis via Co–N$_4$–C intensified radical and nonradical pathways. *Environ. Sci. Technol.* **56**, 11635–11645 (2022).
26. M. Zhang *et al.*, Selective oxidation of organic pollutants based on reactive oxygen species and the molecular structure: Degradation behavior and mechanism analysis. *Water. Res.* **246**, 120697 (2023).
27. J. Liu *et al.*, A photo-switch for peroxydisulfate non-radical/radical activation over layered CuFe oxide: Rational degradation pathway choice for pollutants. *Appl. Catal. B Environ.* **261**, 118232 (2020).
28. W. Ren *et al.*, Activation of peroxydisulfate on carbon nanotubes: Electron-transfer mechanism. *Environ. Sci. Technol.* **53**, 14595–14603 (2019).
29. R. Xiao *et al.*, Quantitative structure-activity relationship (QSAR) for the oxidation of trace organic contaminants by sulfate radical. *Environ. Sci. Technol.* **49**, 13394–13402 (2015).
30. T. Ye *et al.*, Chemical structure-based predictive model for the oxidation of trace organic contaminants by sulfate radical. *Water. Res.* **116**, 106–115 (2017).
31. G. V. Buxton, C. L. Greenstock, W. P. Helman, A. B. Ross, Critical Review of rate constants for reactions of hydrated electrons, hydrogen atoms and hydroxyl radicals (·OH/·O$^-$ in aqueous solution. *J. Phys. Chem. Ref. Data* **17**, 513–886 (1988).
32. P. Neta, J. Grodkowski, A. B. Ross, Rate constants for reactions of aliphatic carbon-centered radicals in aqueous solution. *J. Phys. Chem. Ref. Data* **25**, 709–1050 (1996).
33. R. Luo *et al.*, Singlet oxygen-dominated non-radical oxidation process for efficient degradation of bisphenol A under high salinity condition. *Water. Res.* **148**, 416–424 (2019).
34. M. Zhang *et al.*, Confined pyrolysis of metal–organic frameworks to N-doped hierarchical carbon for non-radical dominated advanced oxidation processes. *J. Mater. Chem. A* **7**, 12547–12555 (2019).
35. A. Wang *et al.*, MOF derived Co−Fe nitrogen doped graphite carbon@crosslinked magnetic chitosan Micro−nanoreactor for environmental applications: Synergy enhancement effect of adsorption−PMS activation. *Appl. Catal. B Environ.* **319**, 121926 (2022).
36. C. Chen *et al.*, In-situ pyrolysis of Enteromorpha as carbocatalyst for catalytic removal of organic contaminants: Considering the intrinsic N/Fe in Enteromorpha and non-radical reaction. *Appl. Catal. B Environ.* **250**, 382–395 (2019).
37. H. C. Li, C. Shan, B. C. Pan, Fe(III)-doped g-C$_3$N$_4$ mediated peroxymonosulfate activation for selective degradation of phenolic compounds via high-valent iron-oxo species. *Environ. Sci. Technol.* **52**, 2197–2205 (2018).
38. Y. Zong *et al.*, Do we appropriately detect and understand singlet oxygen possibly generated in advanced oxidation processes by electron paramagnetic resonance spectroscopy?. *Environ. Sci. Technol.* **57**, 9394–9404 (2023).
39. M. Li *et al.*, Degradation of various thiol collectors in simulated and real mineral processing wastewater of sulfide ore in heterogeneous modified manganese slag/PMS system. *Chem. Eng. J.* **413**, 127478 (2021).
40. Y. Zong *et al.*, Unraveling the overlooked involvement of high-valent cobalt-oxo species generated from the cobalt(II)-activated peroxymonosulfate process. *Environ. Sci. Technol.* **54**, 16231–16239 (2020).
41. H. Li, Z. Zhao, J. Qian, B. Pan, Are free radicals the primary reactive species in Co(II)-mediated activation of peroxymonosulfate? New evidence for the role of the Co(II)–peroxymonosulfate complex. *Environ. Sci. Technol.* **55**, 6397–6406 (2021).
42. N. Jiang, H. Xu, L. Wang, J. Jiang, T. Zhang, Nonradical oxidation of pollutants with single-atom-Fe(III)-activated persulfate: Fe(V) being the possible intermediate oxidant. *Environ. Sci. Technol.* **54**, 14057–14065 (2020).
43. H. Li *et al.*, Persulfate adsorption and activation by carbon structure defects provided new insights into ofloxacin degradation by biochar. *Sci. Total Environ.* **806**, 150968 (2022).
44. A. Kugler *et al.*, Reductive defluorination of Perfluorooctanesulfonic acid (PFOS) by hydrated electrons generated upon UV irradiation of 3-Indole-acetic-acid in 12-Aminolauric-Modified montmorillonite. *Water Res.* **200**, 117221 (2021).
45. X. Peng *et al.*, Activation of peroxymonosulfate by single atom Co-N-C catalysts for high-efficient removal of chloroquine phosphate via non-radical pathways: Electron-transfer mechanism. *Chem. Eng. J.* **429**, 132245 (2022).
46. T. Ye *et al.*, Quantitative structure–activity relationship for the apparent rate constants of aromatic contaminants oxidized by ferrate (VI). *Chem. Eng. J.* **317**, 258–266 (2017).
47. Y. Gao *et al.*, Activity trends and mechanisms in peroxymonosulfate-assisted catalytic production of singlet oxygen over atomic metal-N-C catalysts. *Angew. Chem. Int. Ed.* **60**, 22513–22521 (2021).
48. K. Yin *et al.*, Redox potentials of pollutants determining the dominate oxidation pathways in manganese single-atom catalyst (Mn-SAC)/peroxymonosulfate system: Selective catalytic mechanisms for versatile pollutants. *Appl. Catal. B Environ.* **338**, 123029 (2023).
49. M. Luo *et al.*, Efficient activation of ferrate(VI) by colloid manganese dioxide: Comprehensive elucidation of the surface-promoted mechanism. *Water Res.* **215**, 118243 (2022).
50. Y. Chai *et al.*, Selective degradation of organic micropollutants by activation of peroxymonosulfate by Se@NC: Role of Se doping and nonradical pathway mechanism. *J. Hazard. Mater.* **452**, 131202 (2023).
51. Z. Wei *et al.*, Electrophilicity index as a critical indicator for the biodegradation of the pharmaceuticals in aerobic activated sludge processes. *Water Res.* **160**, 10–17 (2019).
52. P. Shao *et al.*, Potential difference driving electron transfer via defective carbon nanotubes toward selective oxidation of organic micropollutants. *Environ. Sci. Technol.* **54**, 8464–8472 (2020).
53. W. Ren *et al.*, Insights into the electron-transfer regime of peroxydisulfate activation on carbon nanotubes: The role of oxygen functional groups. *Environ. Sci. Technol.* **54**, 1267–1275 (2020).
54. F. Chen *et al.*, Single-atom iron anchored tubular g-C$_3$N$_4$ catalysts for ultrafast fenton-like reaction: Roles of high-valency iron-oxo species and organic radicals. *Adv. Mater.* **34**, 2202891 (2022).
55. Y. Chai *et al.*, Elucidation of the mechanistic origin of spin-state-dependent P-doped Fe single-atom catalysts for the oxidation of organic pollutants through peroxymonosulfate activation. *Appl. Catal. B Environ.* **341**, 123289 (2024).
56. J. Xu *et al.*, Organic wastewater treatment by a single-atom catalyst and electrolytically produced H$_2$O$_2$. *Nat. Sustain.* **4**, 233–241 (2021).
57. Y. J. Zhang *et al.*, Simultaneous nanocatalytic surface activation of pollutants and oxidants for highly efficient water decontamination. *Nat. Commun.* **13**, 3005 (2022).